Epitaxial growth of Al-Cr-N thin films on MgO(111)

H. Willmann, M. Beckers, J. Birch, P.H. Mayrhofer, C. Mitterer, and L. Hultman

Epitaxial growth of Al-Cr-N thin films on MgO(111)

H. Willmann[1,2], M. Beckers[2], J. Birch[2], P.H. Mayrhofer[3], C. Mitterer[3], L. Hultman[2]

[1] Materials Center Leoben, 8700 Leoben, Austria

[2] IFM Material Physics, Division of Thin Film Physics, Linköping University, 58183 Linköping, Sweden

[3] Department of Physical Metallurgy and Materials Testing, University of Leoben, 8700 Leoben, Austria

Abstract

Cubic rock salt structure $Al_{0.60}Cr_{0.40}N$ and $Al_{0.68}Cr_{0.32}N$ films of different thicknesses were grown epitaxially onto MgO(111) substrates by reactive unbalanced magnetron sputtering at 500°C. Rutherford backscattering spectroscopy reveals stoichiometric nitrides with Al/Cr ratios close to the ones of the used compound targets of 60/40 and 70/30. High resolution x-ray diffraction proves epitaxial growth over the whole film thickness up to thicknesses of ~1.8 µm. Reciprocal space maps and selected area electron diffraction show that the $Al_xCr_{1-x}N$ films grow fully relaxed. Scanning and transmission electron microscopy imaging reveals columnar microstructures with column widths between 12–16 nm and {001} surface faceting on individual columns. The fully relaxed growth and the columnar structure can be attributed to limited ad-atom mobility on the initial $Al_xCr_{1-x}N(111)$ growth surface.

Keywords: AlCrN, CrAlN, coherence length, mosaicity, wurtzite structure, epitaxy

1. Introduction

Ternary nitrides are used in a wide range of applications from semiconductors to protective hard coatings. The binary nitrides AlN and CrN with wurtzite and rock salt crystallographic structures, respectively, exhibit very low solubility for each other in the thermodynamic equilibrium, even at 1000°C [1]. This miscibility gap can, however, be overcome by physical vapor deposition (PVD) techniques with the formation of metastable $Al_xCr_{1-x}N$ solid solutions in crystallographic modifications of the corresponding binary systems, where Al and Cr atoms are substituting each other [2-9]. Depending on the desired application, thin film synthesis in the AlN-CrN system is approached from two sides of the pseudobinary phase diagram. Starting from hexagonal (wurtzite, B4) AlN, substitution by Cr leads to wurtzite $Al_xCr_{1-x}N$ (w-$Al_xCr_{1-x}N$) which is applied for band gap engineering and the production of dilute magnetic semiconductors in the field of spintronics [10-15]. Vice versa, alloying cubic (rock salt, B1) CrN with Al results in rock salt structure $Al_xCr_{1-x}N$ (c-$Al_xCr_{1-x}N$) with improved mechanical properties [2-6]. This opens up opportunities for cutting applications, in particular for Al contents close to the maximum supersaturation for the B1/B4 transition in PVD films at x=0.7-0.75 [2-5, 16].

Both binary systems, CrN and AlN, have been grown as epitaxial single layers in their native B1 and B4 structure modifications, respectively [17, 18]. However, up to date, only polycrystalline ternary c-$Al_xCr_{1-x}N$ thin films have been studied. Here we present results on epitaxial c-$Al_xCr_{1-x}N$ films with compositions deep within the miscibility gap. They were deposited by reactive unbalanced magnetron sputtering onto single-crystal MgO(111) templates. MgO also crystallizes in the rock salt structure and exhibits only a small lattice mismatch of +2.5% for the investigated c-$Al_xCr_{1-x}N$ films with $0.60 < x < 0.68$.

2. Experimental details

All films were grown in a high-vacuum deposition system equipped with two planar unbalanced magnetrons tilted by 25° to the substrate normal. A detailed description of the system is given elsewhere [19, 20]. For the deposition of the $Al_xCr_{1-x}N$ films, only one magnetron was used, mounted with Al/Cr compound targets with atom ratios of 60/40 or 70/30, respectively. The substrates were positioned on a rotating multi-specimen substrate holder, symmetrically around its rotation axis to achieve uniform film properties. The distance between the substrates and the Ø 75 mm target was 92 mm. The base pressure of the chamber was 2.67×10^{-4} Pa (2×10^{-6} Torr), achieved using a 510 $l\cdot s^{-1}$ turbomolecular pump. The reactive sputtering was carried out in a pure N_2 (99.999 %) atmosphere at a pressure of 0.4 Pa (3×10^{-3} Torr), measured by a capacitance manometer.

Polished MgO(111) wafers of $10\times10\times0.5$ mm^3 size with an average roughness (R_a) of 0.114 nm were used as templates for the films. Additionally, equally sized pyrolytic graphite substrates were used for detailed compositional evaluation. Prior to deposition, the MgO(111) substrates were degassed and cleaned by holding ~750°C for 60 min. During deposition, the substrates were kept at a constant temperature of 500°C, measured by a calibrated pyrometer on an $Al_xCr_{1-x}N$ coated dummy substrate. After cooling down to room temperature the samples were removed from the deposition chamber via a load lock system.

The magnetron was operated at 0.75 A using a constant current regulation, resulting in steady discharge voltages of 370 V and 330 V for the 60/40 and 70/30 target, respectively. In order to provide low-energy ion bombardment during growth, a substrate bias of -40 V was applied. Before starting the deposition, the target was plasma etched for 3 min with the substrates protected by a shutter. The influence of the film thickness on the developed microstructure was addressed by samples grown with different deposition times (10, 60, and 180 min) to cover film thicknesses from below 100 to more than 1000 nm.

The chemical composition of the films was analyzed by Rutherford backscattering spectroscopy (RBS) with a beam of 2 MeV $^4He^+$ ions impinging at an incidence angle of 7° with respect to the surface normal, and being detected at a scattering angle of 167°. The recorded spectra were evaluated using the SIMNRA code [21]. For improved nitrogen quantification, also films deposited onto pyrolytic graphite in corresponding batches were measured, so that the maximum error for nitrogen is ~2 at%, while it is ~1 at% for the heavier Al and Cr.

Structural characterization by high-resolution symmetric x-ray diffraction (HR-XRD), rocking curves, and reciprocal space maps (RSM) was performed using a Philips X'pert MRD triple axis diffractometer equipped with a Cu lab-source. The used optics were a parabolic graded multilayer mirror collimator, followed by a channel-cut 2-bounce Ge (220) monochromator on the primary side and an asymmetric 2-bounce Ge (220) analyzer crystal on the secondary side resulting in Cu-K_α monochromacy of $\Delta\lambda/\lambda = 4.183\times10^{-4}$. Symmetric and asymmetric RSMs were recorded around the MgO 111 and MgO 113 reciprocal lattice points, respectively. In-plane and out-of-plane lattice spacings were evaluated from both RSMs, with the asymmetric 113 RSM being projected onto the [111] and [110] crystallographic axes. Azimuthal XRD scans recorded on the film and substrate 002 reflections were measured with an open detector at a tilt of 54.7° with respect to the diffraction plane (Ψ-tilt).

A Zeiss EVO 50 scanning electron microscope (SEM) equipped with a tungsten filament was used to study the developing morphology by plan-view and fracture cross-section investigations in dependence of the film thickness.

Cross-sectional transmission electron microscopy (TEM) was performed on a Tecnai G^2 TF 20 UT microscope operating at 200 keV for detailed studies of the microstructure. The specimens were prepared by mechanical grinding and polishing before dimpling and a final ion milling step with Ar-ions in a Gatan precision ion polishing system.

3. Results and discussion

The RBS investigations reveal stoichiometric nitrides with an (Al+Cr)/N ratio of 1.00 for all films. The Al/Cr ratios are homogeneous over the whole film thickness and close to the ones of the corresponding targets, with chemical compositions of $Al_{0.60}Cr_{0.40}N$ and $Al_{0.68}Cr_{0.32}N$ for the 60/40 and 70/30 targets. Assuming bulk atomic CrN density, the fitted RBS spectra yield deposition rates of 9.7 and 4.9 nm/min for the 60/40 and 70/30 targets, respectively. The deposition times of 10, 60, and 180 min result in total thicknesses of 100, 580, and 1750 nm for the $Al_{0.60}Cr_{0.40}N$ and 50, 300, and 900 nm for the $Al_{0.68}Cr_{0.32}N$ films. Despite identical deposition currents, the different composition affects the target poisoning during the reactive sputtering. The more likely poisoning of the Al results in a lower discharge voltage, hence a lower total power and therefore significantly reduced deposition rate for the 70/30 setup.

Overview conventional XRD 2θ−ω scans from 25-85° indicate single-phase c-$Al_xCr_{1-x}N$ films, with corresponding MgO and c-$Al_xCr_{1-x}N$ $\ell\ell\ell$ peaks. No w-$Al_xCr_{1-x}N$ phase was observed, despite the potential epitaxial relationship of $(111)_{MgO}\|(0001)_{w\text{-}AlCrN}$ and $[1\bar{1}0]_{MgO}\|[\bar{1}2\bar{1}0]_{w\text{-}AlCrN}$. HR-XRD was used to investigate the region $34° \leq 2\theta \leq 50°$, covering the c-$Al_xCr_{1-x}N$ and MgO 111 and 002 peak positions, respectively. Figures 1a and 1c show the corresponding 2θ-ω scans of c-$Al_{0.60}Cr_{0.40}N$ and c-$Al_{0.68}Cr_{0.32}N$ films for different thicknesses. Samples with 180 min deposition time are comparable in peak position and intensity to the corresponding 60 min samples and for reasons of clarity not displayed in Fig. 1. The peak center positions lie at 2θ values of ~36.94° for MgO 111, at ~37.83° for c-$Al_{0.60}Cr_{0.40}N$ 111, and at ~38.05° for c-$Al_{0.68}Cr_{0.32}N$ 111. Only negligible traces of a c-$Al_{0.60}Cr_{0.40}N$ 002 peak at ~43.5° can be observed.

.

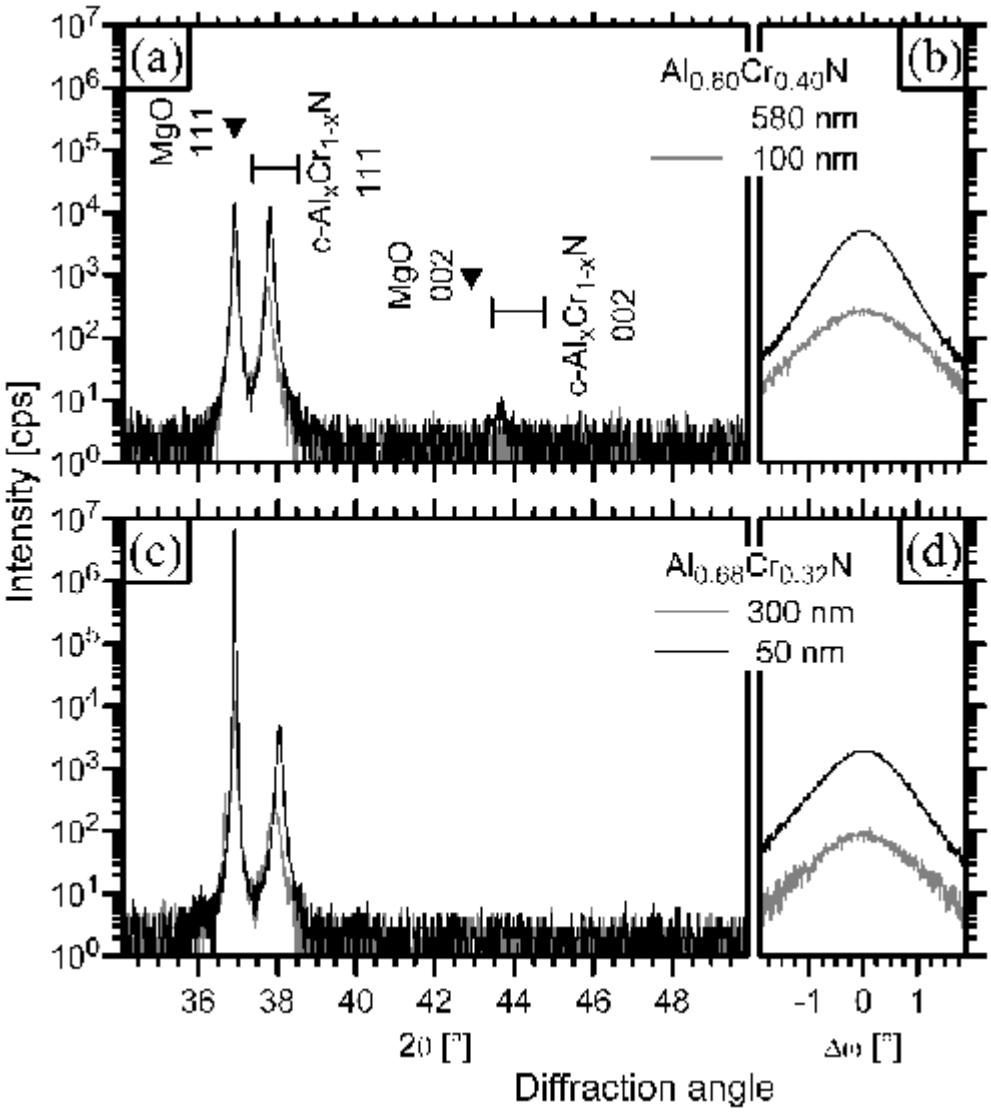

Fig. 1. HR-XRD scans of $Al_{0.60}Cr_{0.40}N$ (a) and $Al_{0.68}Cr_{0.32}N$ films (c) with the corresponding rocking curves (b) and (d), respectively, recorded at the position of maximum 2θ intensity. The theoretical positions for MgO [22] are indicated with a triangle, a range for c-$Al_xCr_{1-x}N$ is indicated with boarders corresponding to CrN [17] and c-AlN [22].

The out-of-plane lattice parameters calculated from the values above result in 4.211 Å for MgO, which corresponds well to the literature value of 4.211 Å [22]. The c-$Al_xCr_{1-x}N$ lattice parameters depend on the Al content as shown for polycrystalline coatings [3-6, 8]. Here, the calculated lattice parameters are 4.116 Å for the $Al_{0.60}Cr_{0.40}N$ and 4.093 Å for the $Al_{0.68}Cr_{0.32}N$ films, which are in good agreement with reported values. Via the Scherrer formula ($\xi_{\perp}=\lambda/(2\Gamma_{2\theta-\omega}\cos\theta)$) the peak full widths at half maximum (FWHM) in 2θ-ω scan direction ($\Gamma_{2\theta-\omega}$) can be used as a measure for the vertical size of coherently scattering

volumes $\xi_\perp$ [17, 23-25]. Smaller values indicate fewer defects, and/or a larger crystal size along the growth direction. The $\Gamma_{2\theta-\omega}$ values for the bulk MgO single crystal substrates are likely to be smaller in comparison to the $\Gamma_{2\theta-\omega}$ values of the films, whose maximum vertical size of coherently scattering volumes is limited by the film thickness. Disregarding the influence of microstrain the values are $\xi_\perp$=120 nm ($\Gamma_{2\theta-\omega}$ = 0.08°) for the 580 nm and 1750 nm thick $Al_{0.60}Cr_{0.40}N$ films and 54 nm ($\Gamma_{2\theta-\omega}$ = 0.17°) for the 100 nm thick $Al_{0.60}Cr_{0.40}N$. For the 300 nm and 900 nm thick $Al_{0.68}Cr_{0.32}N$ films $\xi_\perp$=85 nm ($\Gamma_{2\theta-\omega}$ = 0.11°), and $\xi_\perp$=38 nm ($\Gamma_{2\theta-\omega}$ = 0.24°) for the 50 nm $Al_{0.68}Cr_{0.32}N$ thick film is obtained. The trend of decreasing $\xi_\perp$/thickness ratio with increasing film thickness is due to growing influence of the instrumental broadening. The $\xi_\perp$ values for the thicker films (deposition time 60 and 180 min), are within the range of the calculated $\xi_\perp$ values for the bulk single-crystal MgO substrate value of 150 nm ($\Gamma_{2\theta-\omega}$ = 0.04°). It can therefore be concluded that the size of coherently scattering volumes lies within the range of the film thickness and that contribution of structural defaults, and hence microstrain is negligible. This in turn justifies the use of the simple Scherrer equation to evaluate $\xi_\perp$.

Figures 1b and 1d display rocking curves (ω-scans) over the 111 c-$Al_xCr_{1-x}N$ film peaks that correspond to the 2θ-ω scans of Figs. 1a and 1c. Absolute values for the FWHM Γ_ω of the thickest films are Γ_ω = 0.87° for the $Al_{0.60}Cr_{0.40}N$ 111 peak and Γ_ω = 1.11° for the $Al_{0.68}Cr_{0.32}N$ 111 peak. These Γ_ω values are higher compared to previously reported values for epitaxial layers of rock salt structure binary nitrides with comparable lattice mismatch, like 0.14° for TiN [23], 0.15° for CrN [17], or 0.6° for TaN [26]. Also materials that exhibit significantly larger lattice mismatches to MgO like HfN (Δa~7.5%) and ScN (Δa~7%) show smaller Γ_ω of 0.58° [24] and 0.87° [25], respectively. Γ_ω is among other factors influenced by the lateral size of coherently scattering volumes $\xi_{||}$, strain due to dislocations and mosaicity [27]. Rocking curves on the $Al_{1-x}Cr_xN$ 222 peaks, not shown, reveal that in reciprocal space

the FWHM in q_x direction Γ_{qx} for $Al_{1-x}Cr_xN$ 111 is smaller than for $Al_{1-x}Cr_xN$ 222. This implies a contribution of $\xi_{||}$ and mosaicity, since for pure lateral coherence length influence Γ_{qx} 111 and Γ_{qx} 222 should be the same according to the mosaic block model of epitaxial films [28].

The higher Γ_ω values of the present c-$Al_xCr_{1-x}N$ films can hence be explained by either lower lateral coherence length or increased strain and mosaicity. The latter one is mainly linked to the formation of dislocations, and hence lattice-mismatch dependent. Therefore different film materials can not directly be compared. Even for the same film material a reduced lateral coherence length can be induced by the choice of the substrate. The MgO(111) templates used for epitaxial growth in this work for example provide a less stable heteropolar surface resulting in higher defect densities compared to the low energy MgO(001) surface used in the other studies [17, 23-26]. Also, a c-$Al_xCr_{1-x}N$ (111) growth plane provides three backbonds, which drastically decreases the ad-atom surface mobility. This influence is further aggravated by the lower substrate temperature employed in the present study.

The epitaxial relations between the MgO substrate and the $Al_{0.60}Cr_{0.40}N$ and $Al_{0.68}Cr_{0.32}N$ films were further investigated by 360° azimuthal scans over the 002 peaks (Fig. 2). The scans were performed at $2\theta = 44.055°$ for the $Al_{0.60}Cr_{0.40}N$ (Fig. 2a), 44.287° for the $Al_{0.68}Cr_{0.32}N$ sample (Fig. 2b), and 42.930° for the MgO substrate (Fig. 2c), and prove the cube-on-cube epitaxial relation $(111)_{MgO}||(111)_{c\text{-}AlCrN}$ and $[110]_{MgO}||[110]_{c\text{-}AlCrN}$ since the film intensity maxima lie at identical azimuthal angles as the (111) substrate peaks. Additional to the threefold substrate peaks Figs. 2a and 2b also display a second threefold symmetry with peaks of minor intensities at an azimuthal shift of 60°. These contributions are due to the existence of either double positioning domains [29] or stacking faults/microtwins on the (111) planes. However, their low 0.5% intensity ratio to the main epitaxial peaks indicates a marginal quantity that can only be seen with the open detector setup and on the logarithmic scale.

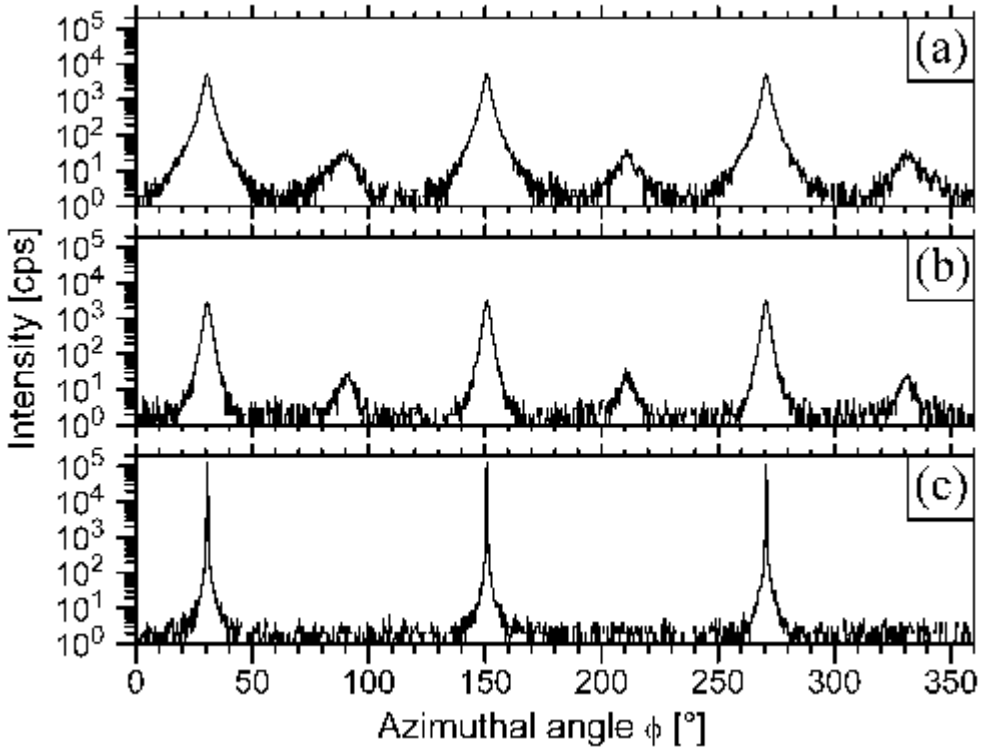

Fig. 2. Azimuthal XRD scans for Ψ=54.7° on the 002 reflections of epitaxial $Al_{0.60}Cr_{0.40}N$ (a) and $Al_{0.68}Cr_{0.32}N$ films (b) as well as from the MgO(111) substrate (c).

Figure 3 shows RSMs recorded around the 113 MgO reciprocal lattice points for films of both compositions, with q_z and q_x aligned along [001] and [110]. The measured intensities of the 580 nm thick $Al_{0.60}Cr_{0.40}N$ and the 300 nm thick $Al_{0.68}Cr_{0.32}N$ films and the corresponding MgO substrates are displayed in Figs. 3a and 3b, respectively. The arrowed lines indicate the direction of the reciprocal lattice vector. Both film intensity distributions are centered on this line suggesting fully relaxed growth during the deposition process [30, 31]. Consequently, the calculated in-plane ($a_{\|}$) and out-of-plane ($a_{\perp}$) lattice parameters are identical within the accuracy of the measurement. Absolute values are $a_{\|}=a_{\perp}=4.211$ Å for MgO, $a_{\|}=4.116$ and $a_{\perp}=4.117$ Å for $Al_{0.60}Cr_{0.40}N$, as well as $a_{\|}=4.095$ and $a_{\perp}=4.096$ Å for $Al_{0.68}Cr_{0.32}N$. These values correspond well to the results from the 2θ-ω diffraction data in Figs. 1a and 1c. Differences in maximum intensities can be explained by the lower thickness of the $Al_{0.68}Cr_{0.32}N$ compared to the $Al_{0.60}Cr_{0.40}N$ film. Also, the intensity distributions of the films

lie essentially perpendicular to the reciprocal lattice vector, indicating a minor influence of $\xi_{||}$, but mainly broadening due to mosaicity.

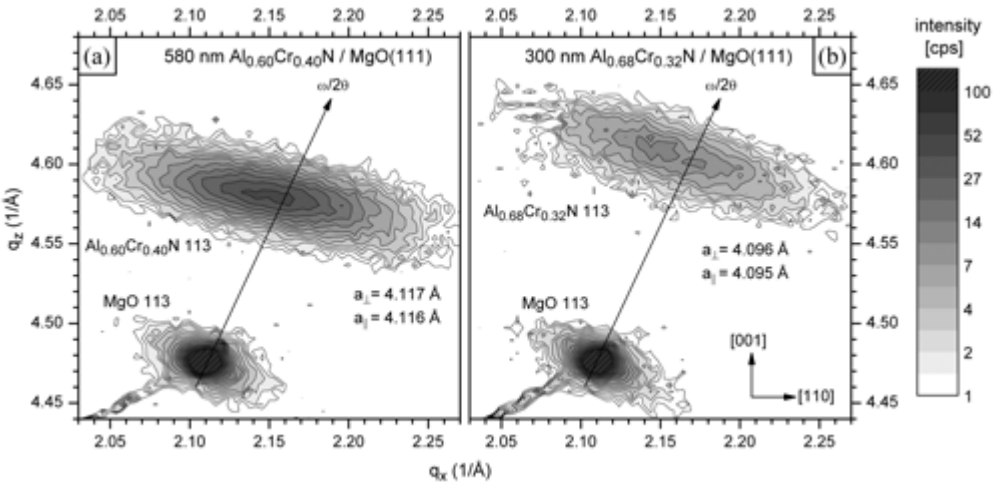

Fig. 3. Asymmetric RSMs around the MgO 113 reciprocal lattice point for epitaxial $Al_{0.60}Cr_{0.40}N$ (a) and $Al_{0.68}Cr_{0.32}N$ films (b) grown on MgO(111). The intensity contours are projected into the plane with the orthogonal directions [001] and [110].

In conclusion, the x-ray investigations suggest fully relaxed growth of the $Al_{0.60}Cr_{0.40}N$ and $Al_{0.68}Cr_{0.32}N$ films with the vertical size of coherently scattering volumes extending over almost the full film thicknesses of 1750 nm and 900 nm, respectively.

To further evaluate the film microstructure, SEM images were obtained of which Fig. 4 exemplary displays (a) the fracture cross-section and (b) the top view from the 1750 nm thick $Al_{0.60}Cr_{0.40}N$ film. The cross-section reveals the fracture of the MgO substrate along the {001} cleavage planes and also illustrates a fibrous columnar structure of the film, which has cracked along boundaries in between individual columns. The column tips exhibit growth facets that are clearly visible in the top view of Fig. 4b. These cube corner shaped surface facets formed by three {001} planes around the [111] direction has been reported in literature before for rock salt structures grown with (111) texture [32]. SEM investigations of $Al_{0.60}Cr_{0.40}N$ films with different film thicknesses revealed full development of these facets already after 50 nm, followed by a steady-state growth condition with little competition for

growth between individual columns as is suggested also by their upright boundaries in Fig 4a. Areas of bigger facets seen in Fig. 4b can be related to surface defects of the initial MgO substrate [33, 34].

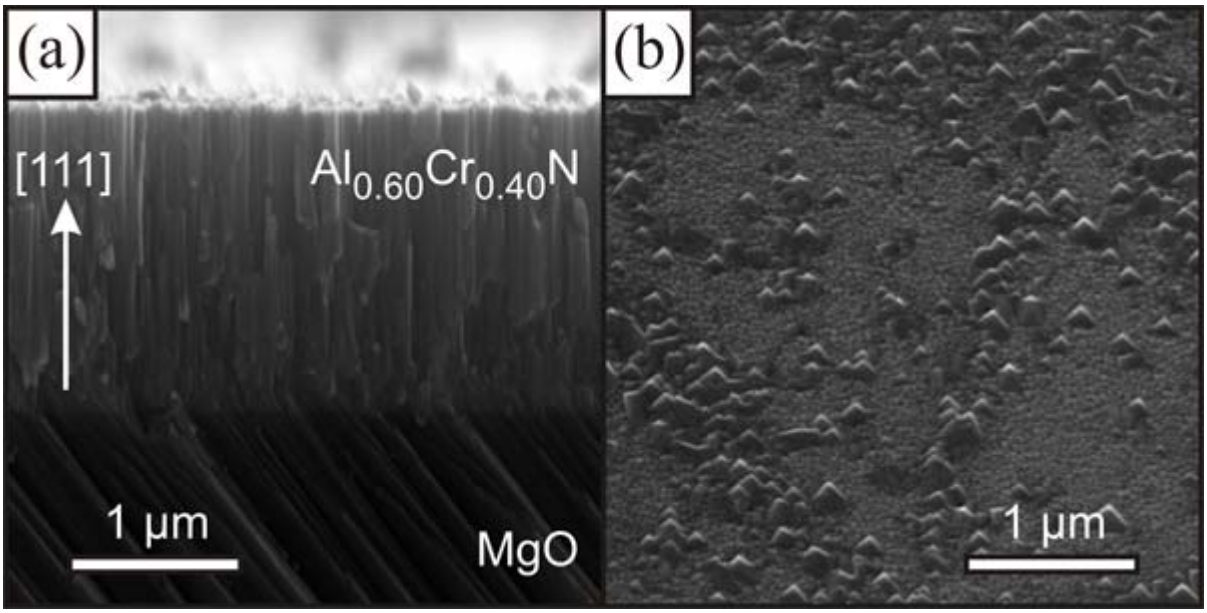

Fig. 4. SEM micrographs of fracture cross-section (a) and top view (b) of a 1750 nm thick $Al_{0.60}Cr_{0.40}N$ film grown on MgO(111).

The columnar microstructure is also apparent in cross-sectional TEM (XTEM) as illustrated in Fig. 5a which is an overview image from the 1750 nm thick $Al_{0.60}Cr_{0.40}N$ film. It confirms the HR-XRD results that the vertical size of coherently scattering volumes – i.e. columns – extends over the whole film thickness. Figure 5b shows the interface region of the 900nm thick $Al_{0.68}Cr_{0.32}N$ sample which already features a columnar structure. The magnified view in Fig. 5c, however, reveals that the columns with ~12 nm are slightly narrower compared to the $Al_{0.60}Cr_{0.40}N$ film with ~16 nm. These column widths match the average diffusion path length on the $Al_{1-x}Cr_xN(111)$ surface of only ~12 nm, calculated based on the applied deposition parameters and theoretical surface binding energies of TiN [35], isostructural to the CrN and $Al_{1-x}Cr_xN$. A different column width for $Al_{0.60}Cr_{0.40}N$ and $Al_{0.68}Cr_{0.32}N$ may be attributed to changed overall mobility with increasing Al content. Taking into account the average lattice constants for MgO (4.211 Å) and $Al_{1-x}Cr_xN$ (4.105 Å), the theoretical distance between two

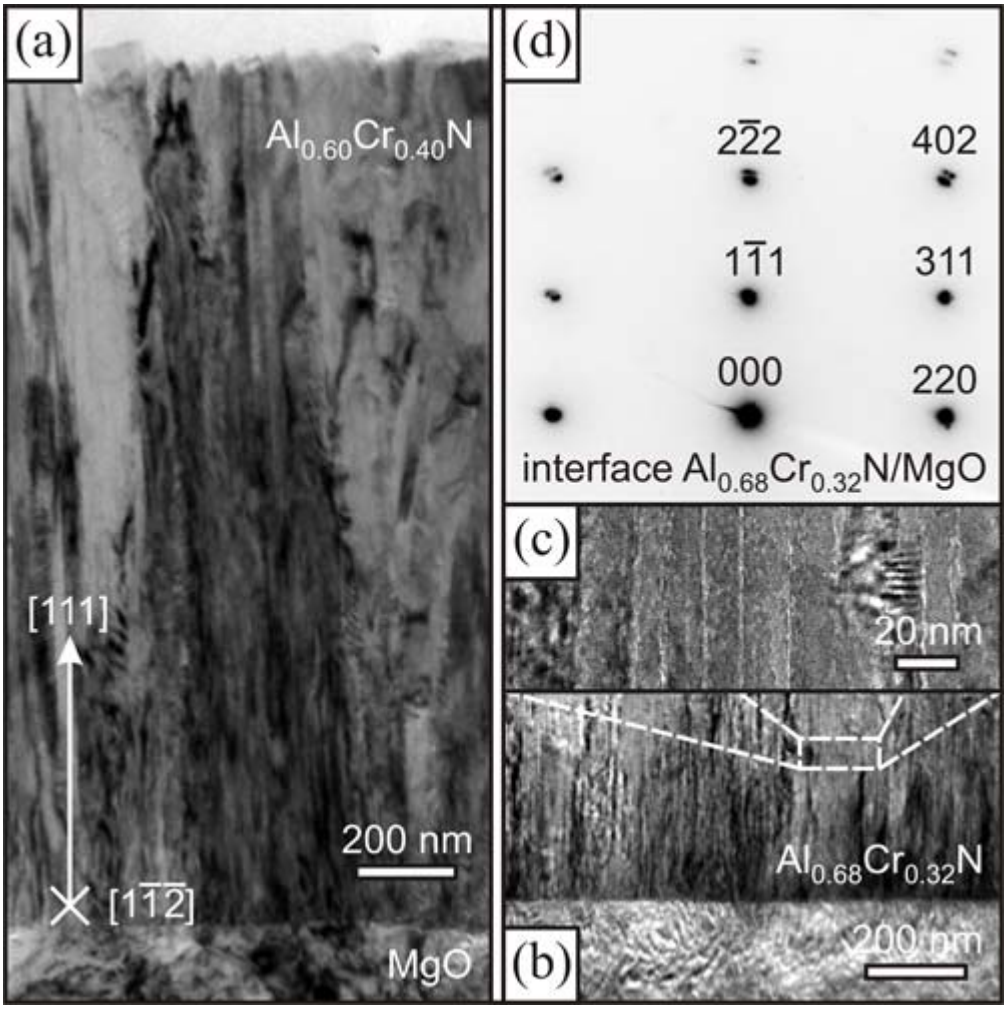

Fig. 5. Cross-sectional TEM micrographs from $Al_{0.60}Cr_{0.40}N$ (a) and $Al_{0.68}Cr_{0.32}N$ (b) films grown on MgO(111) with a magnified view of the columnar structure in (c) and a SAED spot pattern of the interface area in (d).

dislocations is ~39 plane spacings, i.e. ~12 nm along the [1$\bar{1}$0] direction. Hence, the average diffusion path length, the column width and the theoretical dislocation distance all lie in the same range. We therefore conclude that each column is essentially free of any dislocation. Comparable results have been observed for nanocolumnar GaN films grown in a low surface mobility regime [36]. This again justifies the application of the Scherrer formula to calculate $\xi_{\perp}$. The interfacial lattice mismatch between the film and the MgO can be accommodated by voids at the columnar boundaries, which have been described for TiN and NbN epitaxial films before [37]. The voids are detectable in Fig. 5c as regions of lower density along the columns

boundaries. They result from the limited adatom mobility calculated above, which yields a non-planar growth front with surface faceting accompanied by self-shadowing at the film surface cusps. Fig. 5c also illustrates that each column is slightly tilted with respect to the others. Due to their small lateral size the superposition of these tilted crystalline columns in reciprocal space has the same appearance as a tilt of mosaic blocks separated by dislocations, hence this explains the intensity distribution perpendicular to the reciprocal lattice vector in the asymmetric RSMs of Fig. 3. This is also one reason for the broadening of the rocking curve width Γ_ω in Fig. 1.

Figure 5d shows a selected area electron diffraction (SAED) pattern, including the interface region of the $Al_{0.68}Cr_{0.32}N$ sample and the MgO substrate. The distinct spot pattern further confirms epitaxial cube-on-cube relation and the fully relaxed growth mode, since the peak splits of MgO substrate and $Al_{0.68}Cr_{0.32}N$ film, especially seen for higher order reflections like (402), are aligned towards the direct beam spot. From the XTEM analysis also the obtained deposition rates from RBS could be verified.

4. Conclusion

Epitaxial $Al_{0.60}Cr_{0.40}N$ and $Al_{0.68}Cr_{0.32}N$ films can be grown on MgO(111) substrates by reactive unbalanced magnetron sputtering at a deposition temperature of 500°C. The films grow in the rock salt structure with fully relaxed lattice parameters of ~4.116 Å for the $Al_{0.60}Cr_{0.40}N$ and ~4.093 Å for the $Al_{0.68}Cr_{0.32}N$ composition. A self-organized 3D island growth mode with low adatom mobility is observed, resulting in fibrous epitaxial columns. The columns extend over the whole film thickness and exhibit threefold {001} facets on top. The low diffusion path length of only a few nanometer and hence high nucleation density on the initial (111) surface defines the final column width. The observed differences in the

column width between 12 and 16 nm depending on the film composition are likely connected to different Al and Cr adatom mobility on the growth surface.

Acknowledgments

The authors thank F. Eriksson and N. Ghafoor as well as F. Giuliani and D. Trinh (IFM – Thin Film Physics Division, Linköping University) for support regarding the deposition system and the TEM, respectively. The Tandem Accelerator Lab at Uppsala University, Sweden is acknowledged for RBS beamtime. The Christian Doppler Laboratory for Advanced Hard Coatings at the University of Leoben and the Plansee GmbH, Lechbruck, Germany, are acknowledged for providing target materials. Work done in Leoben was financed within the framework of the Austrian Kplus Competence Center Program. The work done in Linköping was financed by the Swedish Research Council (VR) and the Swedish Foundation for Strategic Research (SSF) within the Strategic Research Center MS^2E on Materials Science for Nanoscale Surface Engineering.

Literature:

[1] C. Kunisch, R. Loos, M. Stüber, S. Ulrich, Z. Metallkd. 90 (1999) 847.

[2] H. Hasegawa, M. Kawate, T. Suzuki, Surf. Coat. Technol. 200 (2005) 2409.

[3] Y. Ide, T. Nakamura, K. Kishitake, in: B. Mishra, C. Yamauchi (Eds.), Second International Conference on Processing Materials for Properties, TMS (The Minerals, Metals & Materials Society), San Francisco, 2000, p. 291.

[4] M. Kawate, A. Kimura, T. Suzuki, J. Vac. Sci. Technol. A 20 (2002) 569.

[5] M. Hirai, Y. Ueno, T. Suzuki, W.H. Jiang, C. Grigoriu, K. Yatsui, Jpn. J. Appl. Phys. Part 1 - Regul. Pap. Short Notes Rev. Pap. 40 (2001) 1056.

[6] A.E. Reiter, V.H. Derflinger, B. Hanselmann, T. Bachmann, B. Sartory, Surf. Coat. Technol. 200 (2005) 2114.

[7] Y. Makino, Surf. Coat. Technol. 193 (2005) 185.

[8] P.H. Mayrhofer, H. Willmann, A. Reiter, Proceedings of the Society of Vacuum Coaters 49th annual Technical Conference, Washington, D.C., 04/2006, p. 575.

[9] H. Willmann, P.H. Mayrhofer, P.O.Å. Persson, A.E. Reiter, L. Hultman, C. Mitterer, Scr. Mater. 54 (2006) 1847.

[10] A.Y. Polyakov, N.B. Smirnov, A.V. Govorkov, R.M. Frazier, J.Y. Liefer, G.T. Thaler, C.R. Abernathy, S.J. Pearton, J.M. Zavada, Appl. Phys. Lett. 85 (2004) 4067.

[11] R.M. Frazier, G.T. Thaler, B.P. Gila, J. Stapleton, M.E. Overberg, O.R. Abernathy, S.J. Pearton, F. Ren, J.M. Zavada, J. Electron. Mater. 34 (2005) 365.

[12] D. Kumar, J. Antifakos, M.G. Blamire, Z.H. Barber, Appl. Phys. Lett. 84 (2004) 5004.

[13] Q. Wang, A.K. Kandalam, Q. Sun, P. Jena, Phys. Rev. B 73 (2006) 115411.

[14] A.Y. Polyakov, N.B. Smirnov, A.V. Govorkov, R.M. Frazier, J.Y. Liefer, G.T. Thaler, C.R. Abernathy, S.J. Pearton, J.M. Zavada, J. Vac. Sci. Technol. B 22 (2004) 2758.

[15] S.Y. Wu, H.X. Liu, L. Gu, R.K. Singh, L. Budd, M. van Schilfgaarde, M.R. McCartney, D.J. Smith, N. Newman, Appl. Phys. Lett. 82 (2003) 3047.

[16] W. Kalss, A. Reiter, V. Derflinger, C. Gey, J.L. Endrino, Int. J. Refract. Met. Hard Mater. 24 (2006) 399.

[17] D. Gall, C.S. Shin, T. Spila, M. Odén, M.J.H. Senna, J.E. Greene, I. Petrov, J. Appl. Phys. 91 (2002) 3589.

[18] J. Birch, S. Tungasmita, V. Darakchieva, in: T. Paskova, B. Monemar (Eds.), Vacuum Science and Technology: Nitrides as seen by the technology, Research Signpost, Kerala, 2002, p. 421.

[19] C. Engström, T. Berlind, J. Birch, L. Hultman, I.P. Ivanov, S.R. Kirkpatrick, S. Rohde, Vacuum 56 (2000) 107.

[20] F. Eriksson, G.A. Johansson, H.M. Hertz, J. Birch, Opt. Eng. 41 (2002) 2903.

[21] M. Mayer, Technical Report, Max-Planck-Institut für Plasmaphysik, Garching, Germany, 1997.

[22] Powder Diffraction File (Card 45-0946 for MgO, Card 46-1200 for c-AlN), International Centre for Diffraction Data, ICDD - JCPDS, 1998.

[23] C.S. Shin, S. Rudenja, D. Gall, N. Hellgren, T.Y. Lee, I. Petrov, J.E. Greene, J. Appl. Phys. 95 (2004) 356.

[24] H.S. Seo, T.Y. Lee, J.G. Wen, I. Petrov, J.E. Greene, D. Gall, J. Appl. Phys. 96 (2004) 878.

[25] D. Gall, I. Petrov, N. Hellgren, L. Hultman, J.E. Sundgren, J.E. Greene, J. Appl. Phys. 84 (1998) 6034.

[26] C.S. Shin, D. Gall, P. Desjardins, A. Vailionis, H. Kim, I. Petrov, J.E. Greene, M. Odén, Appl. Phys. Lett. 75 (1999) 3808.

[27] J.E. Ayers, J. Cryst. Growth. 135 (1994) 71.

[28] R. Chierchia, T. Böttcher, H. Heinke, S. Einfeldt, S. Figge, D. Hommel, J. Appl. Phys. 93 (2003) 8918.

[29] Y. Xin, P.D. Brown, C.J. Humphreys, T.S. Cheng, C.T. Foxon, Appl. Phys. Lett. 70 (1997) 1308.

[30] P.v.d. Sluis, J. Phys. D: Appl. Phys. 26 (1993) A188.

[31] M. Birkholz, Thin Film Analysis by X-Ray Scattering, Wiley-VCH Verlag GmbH & Co. KGaA, Weinheim, 2006.

[32] B. Warot, E. Snoeck, J.C. Ousset, M.J. Casanove, S. Dubourg, J.F. Bobo, Appl. Surf. Sci. 188 (2002) 151.

[33] P.W. Tasker, Journal Phys. C Solid State 12 (1979) 4977.

[34] L.E. Toth, Transition Metal Carbides and Nitrides, Academic Press, Inc., New York, 1971.

[35] D. Gall, S. Kodambaka, M.A. Wall, I. Petrov, J.E. Greene, J. Appl. Phys. 93 (2003) 9086.

[36] K.L. Averett, J.E. Van Nostrand, J.D. Albrecht, Y.S. Chen, C.C. Yang, J. Vac. Sci. Technol. B 25 (2007) 964.

[37] L. Hultman, L.R. Wallenberg, M. Shinn, S.A. Barnett, J. Vac. Sci. Technol. A 10 (1992) 1618.